Fault instability on a finite and planar fault related to early phase of nucleation

Yuta Mitsui

Department of Geophysics, Graduate School of Science, Kyoto University, Kyoto, Japan

Kazuro Hirahara

Department of Geophysics, Graduate School of Science, Kyoto University, Kyoto, Japan

Abstract. We numerically investigate the early phase of nucleation on a planar fault with the rate- and state-dependent friction law, loaded externally by steady slip, to clarify its relation to fault instability. We define R_n as the invasion distance of the inward creep to characterize that phase. For a circular fault, the dependence of R_n on the dimensionless parameters l_b, l_{b-a}, and l_{RA} (all of these are proportional to the rigidity and the characteristic distance of the state evolution L and inversely proportional to the normal stress and the fault radius) can be compiled. We found that R_n is proportional to l_b (both aging law and slip law of the state evolution) and l_{b-a} (aging law). In the case of the aging law only, there are two regimes (ordinary events and slow events) separated by the value of l_{RA}. The regimes have different trend lines, although we could not measure R_n for the case of $l_{RA} < 0.35$ because of breaking of the mirror symmetry of instability along the loading direction. R_n in the slow event regime is smaller. Moreover, we investigated the effect of fault shape and found that a model with a long radius along the mode-2 direction has similar parameter dependence to circular faults, but a model with a long radius along the mode-3 direction has different ones. Our results imply that we can qualitatively estimate the fault instability parameters from the early phase of nucleation, although further research is necessary to enable application to actual faults.

1. Introduction

Earthquakes have mainly been observed using elastic wave detectors. Until now, many physical models have focused on underground wave sources, namely, dynamic propagation of high-speed fault slips (dynamic ruptures). The equation of motion is solved in an elastic body with a criterion for stress drop on the fault. Assumptions such as a constant rupture velocity or a linear slip-weakening law (*Ida* [1972]) have been successfully used as criteria for stress drop (*Madariaga* [1976]; *Mikumo and Miyatake* [1978]; *Day* [1982], among many others). The studies showed certain relations between the distribution of initial shear stress, slip velocity, amount of slip, and rupture propagation velocity, as well as the characteristics of elastic wave radiation. However, the models need an early initial condition to initiate dynamic rupture propagation.

Nowadays, in contrast, there are excellent instruments for observation of crustal movement. These instruments can detect even slow fault slips during interseismic, preseismic, and postseismic periods. For example, GPS has already been used to detect a slow slip event with a slip velocity as slow as 10 cm/year (*Miyazaki et al.* [2006]). This indicates the importance of constructing physical models of interseismic, preseismic, and postseismic stress/strain accumulation. In particular, spontaneous nucleation of earthquake sources, which is caused by tectonic forces and is governed by the frictional properties of the fault, has been a target for researchers studying earthquake models. A considerable number of them assume a rate- and state-dependent friction law (*Dieterich* [1979]; *Ruina* [1980]) since it can represent long-term stick-slip behavior with spontaneous nucleation preceding dynamic instability (*Tse and Rice* [1986]; *Lapusta and Rice* [2003]). It can also represent slow interseismic and postseismic deformation (*Marone et al.* [1991]; *Boatwright and Cocco* [1996]; *Liu and Rice* [2005]), as well as dynamic rupture propagation (*Bizzarri et al.* [2001]). Models based on the rate- and state-dependent friction law have been successfully used for simulating all of the above phenomena during an earthquake cycle. Fitting to actual data (using simple models with one degree of freedom) has also been successfully performed (e.g., *Savage and Langbein* [2008]; *Helmstetter and Shaw* [2009]). This study therefore follows the same strategy.

In particular, the dependence of the nucleation parameters on the rate and state friction fault has been investigated in *Dieterich* [1992] as well as in subsequent studies *Rubin and Ampuero* [2005] and *Ampuero and Rubin* [2008]. They assumed a one-dimensional linear fault in a two-dimensional elastic body, loaded via quasi-uniform stress increasing along the entire fault. These studies have shown that nucleation evolves through several stages: (1) localization with a gradual increase in the slip rate, (2) self-acceleration of the slip rate at localized patches, and (3) growth (e.g., crack-like expansion). They have also clarified some dependence of the frictional parameters on nucleation. The characteristic nucleation size depends on a, b, and L, which are the frictional parameters in the rate- and state-dependent friction law, as well as on the rigidity G of the elastic bulk and the effective normal stress $\bar{\sigma}$.

Although the above-mentioned results have contributed to our understanding of nucleation, a number of details remain to be investigated, one of which is the model of stress loading, and another is related to the dimensionality of the parameters. Elaboration of both these points is expected to lead to better understanding of nucleation in actual faults. If we have a means of estimating frictional instability from nucleation, it would be possible to infer fault instability parameters using excellent geodetic instruments such as GPS.

The "early" phase of nucleation (localization) is especially important from this point of view.

Thus, in the present research, we perform numerical experiments to investigate the early phase of nucleation. First, we assume shear stress loading through slip deficits from steady slip, which has been successfully used in models of earthquake recurrence (e.g., *Tse and Rice* [1986]; *Rice* [1993]; *Ben-Zion and Rice* [1995]; *Hori et al.* [2004]), and the Omori aftershock law following stress perturbations (*Kaneko and Lapusta* [2008]). As *Rubin* [2008] discussed in his slow slip simulations, this difference in the stress loading model affects the mechanical equilibrium between the energy release rate and the elastic strain energy. This stress loading model causes the propagation of aseismic slip (hereinafter called "creep") from the edges of the fault and hence leads to dependence of stress accumulation during interseismic periods on the fault size. Next, we prepare a model of a two-dimensional planar fault in a three-dimensional body in accordance with the dynamic rupture models and the earthquake recurrence models in the literature. Naturally, it is extremely difficult to obtain general results about nucleation, even for model faults. As a fundamental step, we assume an isolated fault with a simple geometry, as in *Kato* [2003], which shows the entire cycle of slip events, including the processes of stress accumulation and release in a circular fault patch, by using the rate- and state-dependent friction law and quasi-dynamic approximation (*Rice* [1993]). We do not consider dynamic stress transfer caused by inertial effects (*Chen and Lapusta* [2009]; *Lapusta and Liu* [2009]), even though its importance for earthquake cycles has been demonstrated in *Lapusta and Liu* [2009], since the magnitude of the term must be excessive during high-speed slips with strong wave radiation.

2. Numerical Model

2.1. Basic relations

The relations between the frictional stress τ_f, the loading shear stress τ, the effective normal stress $\bar{\sigma}$, and the slip velocity v at each point are expressed as follows:

$$\tau_f = \bar{\sigma}\mu = \bar{\sigma}\left[\mu_0 + a\ln\left(\frac{v}{v_0}\right) + b\ln\left(\frac{v_0\theta}{L}\right)\right] \tag{1}$$

$$\tau - \tau_f = \frac{Gv}{2c_s} \tag{2}$$

where μ is the frictional coefficient; μ_0 is a reference value corresponding to steady slipping with a reference velocity v_0; a, b, and L are frictional parameters; G is the rigidity; and c_s is the shear wave velocity. Furthermore, θ is a state variable that is equal to L/v for steady slipping and evolves via certain empirical evolution laws (to be described in Section 2.2). At the steady state, $\theta = L/v$, Eq. (1) can be represented as

$$\tau_f = \bar{\sigma}\mu = \bar{\sigma}\left[\mu_0 + (a-b)\ln\left(\frac{v}{v_0}\right)\right] \tag{3}$$

Here, "$a-b$" is well known as an important parameter related to slip instability. A negative value of $a-b$ ($a<b$) is a necessary condition for spontaneous nucleation, although dynamic ruptures or aseismic slips can propagate along the fault even when $a-b$ is positive (e.g.,*Tinti et al.* [2005]; *Perfettini and Ampuero* [2008]). Moreover, on a numerically discretized fault plane, accumulation of the loading stress τ at grid i (x_i, y_i) depends on the fault slip u at all grids. In the case of background fault loading at a rate v_0, τ (x_i, y_i) is calculated from the static response:

$$\tau(x_i,y_i) = \sum_{x_j}\sum_{y_j} K(x_i-x_j, y_i-y_j)[v_0 t - u(x_j,y_j)] \tag{4}$$

where t is the time, and the stiffness kernel K is obtained from the elastostatic theory. To avoid singularities, the grids for τ and u are laid in an overlapping pattern. The right-hand side of Eq. (2) represents the instantaneous stress drop caused by shear wave radiation (*Brune* [1970]; *Rice* [1993]; *Fukuyama and Madariaga* [1998]), which is called the radiation-damping term.

2.2. State evolution laws

As noted in Section 1, it is necessary to use an empirical evolution law for θ in Eq. (1). In this regard, there are two widely used evolution laws (*Dieterich* [1979]; *Ruina* [1983]). One of these is the aging law:

$$\frac{d\theta}{dt} = 1 - \frac{v\theta}{L} \tag{5}$$

and the other is the slip law:

$$\frac{d\theta}{dt} = -\frac{v\theta}{L}\ln\left(\frac{v\theta}{L}\right) \tag{6}$$

Both laws are based on laboratory experiments, and neither can reproduce all experimental results. Because of this imperfectness, a considerable number of numerical studies in this field have used either of the laws as a constitutive law. A composite law is proposed in *Kato and Tullis* [2001], in which the two laws are combined by introducing a cut-off velocity. This law has been used in *Kato* [2003] and several subsequent studies. However, many numerical models with the rate- and state-dependent friction law still assume one of the basic laws (either aging or slip). We therefore assume both basic laws in the present paper.

2.3. Non-dimensionalization and calculation methods

The constitutive Eqs. (1)–(4), together with (5) or (6), can be rendered dimensionless by introducing scaling factors for the length, velocity, and stress parameters. Here, when we introduce three scaling factors (the characteristic size of the fault R for length, v_0 for velocity, and $\bar{\sigma}$ for stress), the constitutive variables and parameters are rendered dimensionless as

$$\begin{aligned} v' = v/v_0, \tau' = \tau/\bar{\sigma}, \tau_f' = \tau_f/\bar{\sigma} = \mu, c_s' = c_s/v_0 \\ G' = G/\bar{\sigma}, K' = KR/\bar{\sigma}, v_0' = v_0/v_0 = 1 \\ t' = tv_0/R, \bar{\sigma}' = \bar{\sigma}/\bar{\sigma} = 1, u' = u/R \\ L' = L/R, x' = x/R, y' = y/R, \theta' = \theta v_0/R \end{aligned}$$

and the constitutive equations are written as

$$\tau_f' = \mu = \mu_0 + a\ln v' + b\ln\left(\frac{\theta'}{L'}\right) \tag{7}$$

$$\tau' - \tau_f' = \frac{G'v'}{2c_s'} \tag{8}$$

$$\tau'(x_i',y_i') = \sum_{x_j'}\sum_{y_j'} K'(x_i'-x_j', y_i'-y_j')[t' - u'(x_j',y_j')] \tag{9}$$

$$\frac{d\theta'}{dt'} = 1 - \frac{v'\theta'}{L'} \quad or \quad \frac{d\theta'}{dt'} = -\frac{v'\theta'}{L'}\ln\left(\frac{v'\theta}{L'}\right) \tag{10}$$

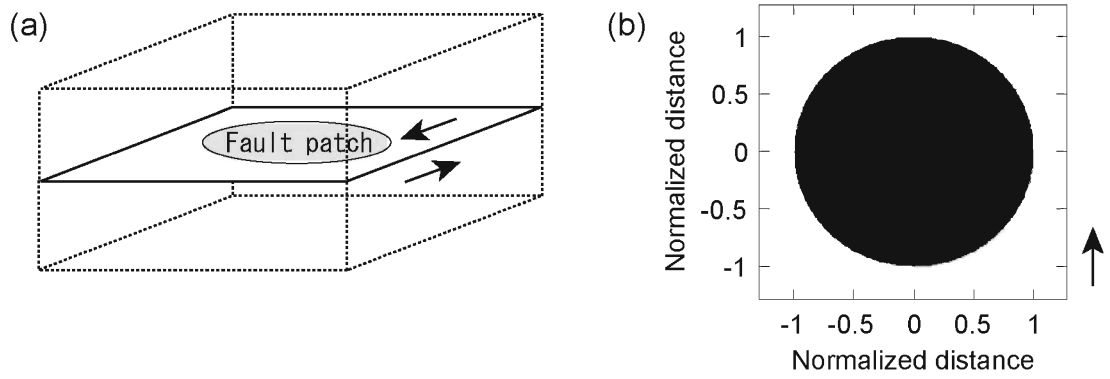

Figure 1. (a) Model in this study: a planar fault in a three-dimensional homogeneous elastic body with a fault patch (with a negative value for $a - b$) and the outside of a steady-slipping region. (b) Cross section along the fault surface representing the lower surface viewed from the top. The black area represents the fault patch, and the arrow indicates the loading direction.

In the calculations, the fault is discretized by introducing a square grid in which the edge size of each square is equal to 0.01 crack radii. Regarding the initial values, we set the steady-state condition as $v' = 0.9$, and $\theta' = L'/0.9$ for the entire grid. In the region of velocity weakening, in order to solve the above constitutive relations, we first differentiate Eqs. (7)–(9) and then integrate them together with Eq. (10) using the RK45 algorithm (*Press et al.* [1992]). Outside the region of velocity weakening, v' is set to become equal to $v' = 1$ soon after the calculation is started. To calculate the loading stress with Eq. (9), we use a two-dimensional FFT method, which entails the introduction of artificial periodic boundary conditions. Although we cannot avoid artificial noise perfectly, as in *Kato* [2003]; *Chen and Lapusta* [2009], the introduction of the steady-slip assumption outside the region of velocity weakening decreases the noise.

2.4. Fault settings

We assume a two-dimensional planar fault in a three-dimensional homogeneous elastic body, and set a circular or elliptical region of velocity weakening (with negative $a - b$). The outside is assumed to have a constant tectonic loading rate (with $v = v_0$), which corresponds to the non-slip boundary condition in classical dynamic rupture models, since we (similar to *Kato* [2003]) implicitly assume a back-slip condition (*Savage* [1983]). This setting is illustrated in Figure 1.

2.5. Model parameters

First, it should be noted that the only explicit parameter for the elastic bulk is $G'/[2c_s']$. This parameter affects only the radiation-damping term, in such a way as to prevent explosion of the slip velocity, and might not significantly affect nucleation. In this study, we use two values for this parameter (1.55×10^{-10} and 1.55×10^{-12}) and confirm that the effect is small. Furthermore, the rigidity G appears implicitly in the elastic kernel K. We tentatively assume that $G = 34.3$ [GPa] and since the rigidity fluctuates relatively little within the seismogenic portion of the crust, the assumption is unlikely to limit the generality of the obtained results.

We also perform numerical experiments by varying the remaining parameters, namely, a, b, and L'. In addition, both state evolution laws are used, as mentioned above. In all cases, the parameter range for which we perform the experiments is $a/b \geq 0.5$, since a and b are considered to be comparable values in terms of the thermally activated rheology of the real contact area (*Nakatani and Scholz* [2004]).

In order to discuss the dependence of the frictional parameters on nucleation, it is preferable to introduce dimensionless parameters for the slip instability. Referring to *Dieterich* [1986], we normalize G/R ($\propto$ effective fault stiffness around the fault center) by some critical values. As a concept, in *Ruina* [1983], the critical stiffness $(b - a)\bar{\sigma}/L$ is obtained by performing linear stability analysis. We next obtain the dimensionless parameter $l_{b-a} = G'L'/(b - a)$. As another concept, in *Dieterich* [1992], it is proposed that nucleation might not depend on $b - a$ but on b alone. We then obtain another dimensionless parameter $l_b = G'L'/b$. In addition, in *Rubin and Ampuero* [2005], one more parameter is introduced, only for the aging law. It is defined as $l_{RA} = l_{b-a}[b/(b - a)] = l_b[b^2/(b - a)^2]$ with non-dimensionalization. Qualitatively, smaller l_{b-a}, l_{b-a}, and l_{RA} result in more unstable fault.

3. Results

3.1. Circular faults

First, we present the results for a simple circular fault. The characteristic fault size R is equal to the fault radius.

3.1.1. In the case of the aging law

In this section, we present the results obtained using the aging law ($d\theta'/dt' = 1 - v'\theta'/L'$).

One set of calculation results is presented in Figure 2, which shows stick-slip behavior after occurrences of several slip events from the initial condition. During the initial phase of the interseismic period, the slip velocity on the entire fault is lower than the loading rate (Figure 2(a); $\log_{10}(v') = 0$ indicates that the slip velocity is equal to the loading rate v_0). The creep front then propagates from outside, leading to spontaneous stress concentration around the fault center. The slip velocity at the creep front increases with its inward propagation. Figures 2(b) and (c) show snapshots of this early phase of nucleation when the maximum value of $\log_{10}(v')$ on the fault exceeds 1 (panel b) and 2 (panel c). Furthermore, Figure 2(d) shows a later phase immediately followed by high-speed slip propagation. After that, the high-speed slip propagates outwards and stops at the fault edge (Figure 2(e)). The slip velocity on the entire fault subsequently decreases and again falls below the loading rate (Figure 2(f)).

Figure 3 shows the same stick-slip behavior via plotting $\Omega = v'\theta'/L'$. The black area represents $\Omega = v'\theta'/L' < 1$, $d\theta'/dt' = 1 - \Omega > 0$ (strengthening); the red area represents $d\theta'/dt' < 0$ (weakening); and the blue area represents $d\theta'/dt' \simeq 0$ (nearly steady state). In panels (a) and (b), the creep front (located at the outer boundary between the red

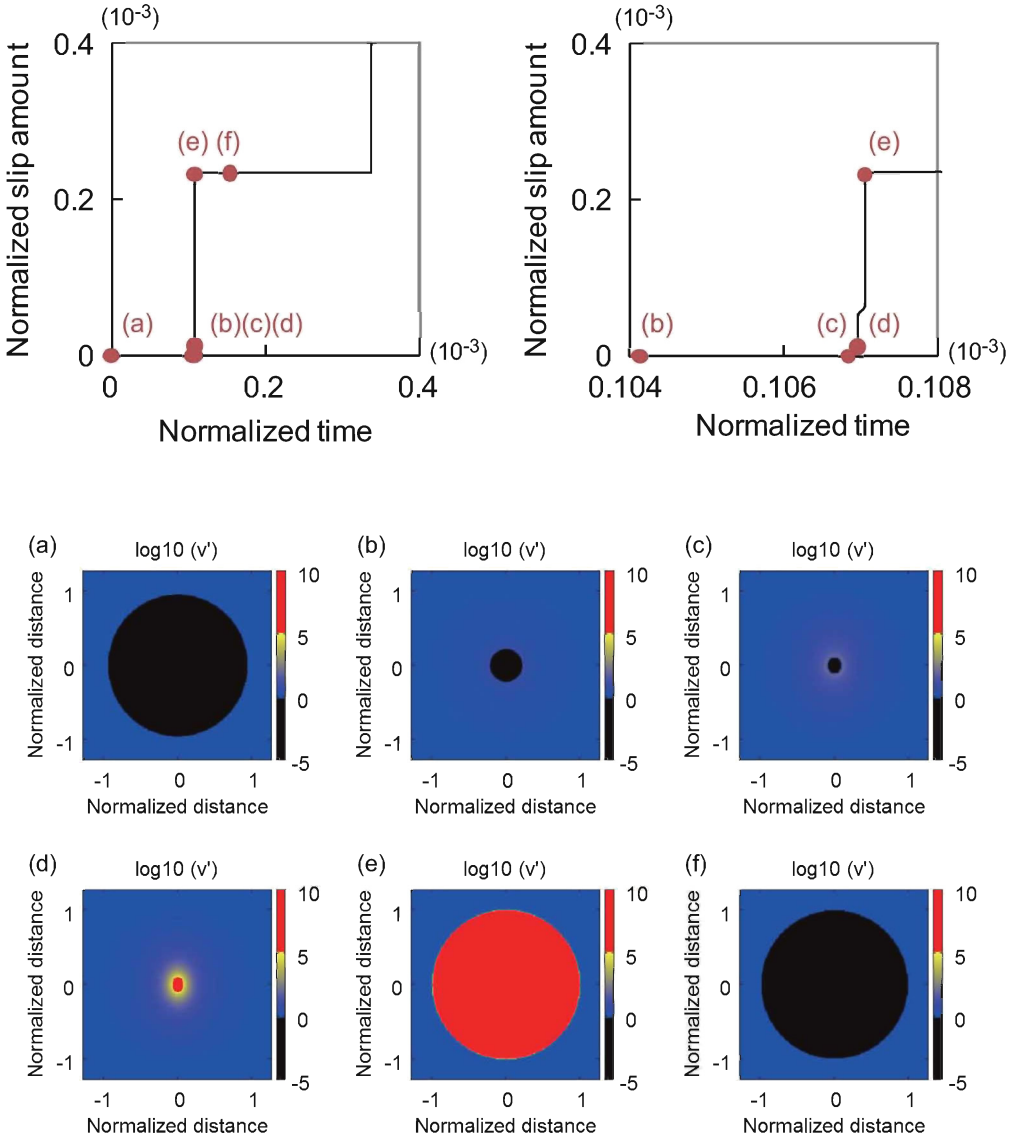

Figure 2. Set of calculation results for the case of the aging law in the OE regime (the definition of this regime is given in Section 3.1.1), with $l_b = 0.037$, $l_{b-a} = 0.16$, and $l_{RA} = 0.694$. In the upper two figures, the solid lines indicate the temporal evolution of the slip at the fault center. The figure on the right is an enlarged version of the figure on the left; the colored points correspond to those in the lower figures and indicate the temporal evolution of the slip velocity, $\log_{10} v'$. The alphabetical order of the six lower figures follows the temporal order in the upper figures. The black region around the fault center in panel (b) represents the area of S_{n1} and in panel (c) represents that of S_{n2}.

and blue areas) is propagating into the black area. In panel (c), the inward creep propagation almost stops, and the slip velocity around the fault center (red area) starts to increase owing to frictional weakening. Thus, at that moment, the early phase of nucleation may finish and the subsequent self-acceleration phase starts. A set of such processes repeats itself on a fixed fault.

In particular, we focus on the early phase of nucleation, as shown in panels (a–c) in Figures 2 and 3. In order to characterize this phase, we measure the "locking center area", with $\log_{10}(v') < 0$, when the maximum value of $\log_{10}(v')$ on the fault exceeds 1, and determine S_{n1} and R_{n1}. S_{n1} is the relative size of the area of the locking center with respect to the entire fault, and $R_{n1} = 1 - \sqrt{S_{n1}}$ approximates the length from the fault edge to the creep front around the locking center area. We also determine S_{n2} and R_{n2}, when the maximum value of $\log_{10}(v')$ on the fault exceeds 2. The relation between S_n and R_n is schematically illustrated in Figure 4.

Extensive calculations were performed by varying the frictional parameters, and the results are reported in Tables 1 and 2. All of the cases show stick-slip behavior. The characteristic sizes (S_{n1}, R_{n1}, S_{n2}, and R_{n2}) in the early phase of nucleation depend on the dimensionless frictional parameters, l_b, l_{b-a}, and l_{RA}, in various ways.

Initially, we classify the results into two regimes: "ordinary events" (OEs) and "slow events" (SEs). We define SEs as the case when the maximum slip velocity v' does not reach $2c_s' a/G'$, which is a characteristic condition of high-speed slip. We can obtain this by differentiating (7) and (8) with respect to t':

$$\left[\frac{G'}{2c_s'} + \frac{a}{v'}\right]\frac{dv'}{dt'} = \frac{d\tau'}{dt'} - \frac{b(d\theta'/dt')}{\theta'} \qquad (11)$$

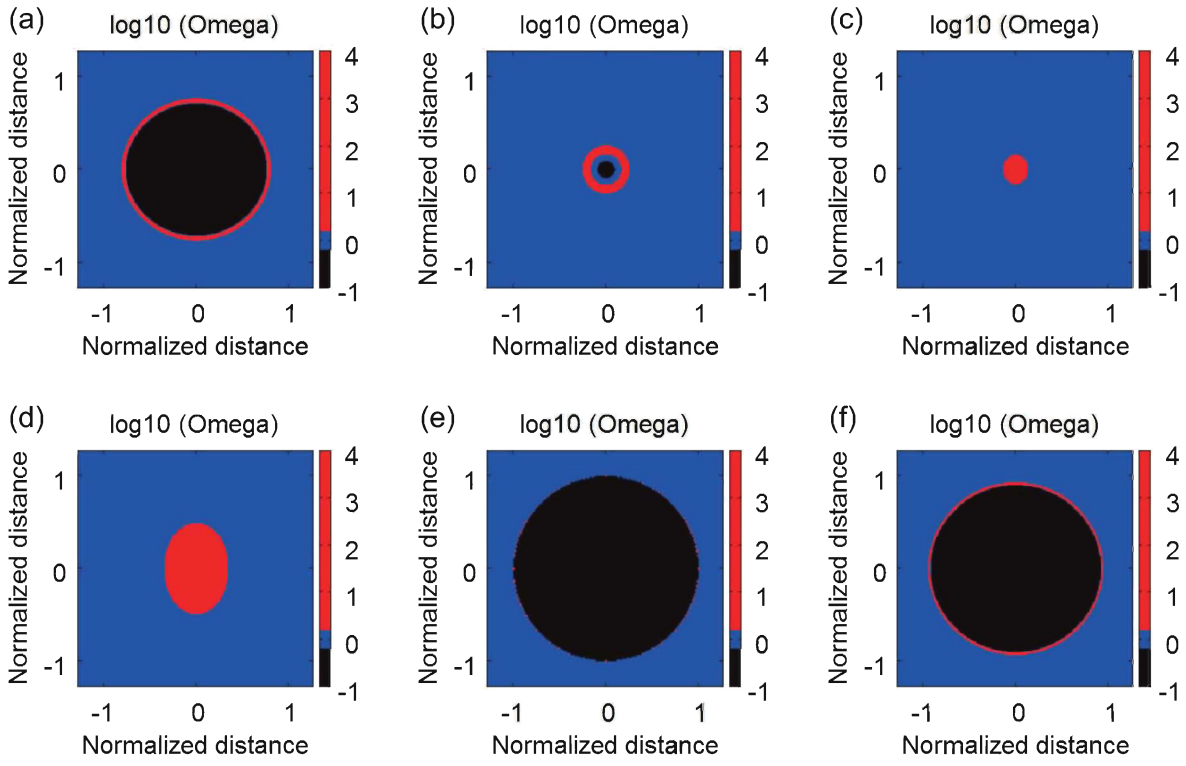

Figure 3. Temporal evolution of $\log_{10}\Omega$ in the same case as in Figure 2. The alphabetical order of the figures follows that in Figure 2. The black area represents $\Omega = v'\theta'/L' < 1$, $d\theta'/dt' = 1 - \Omega > 0$ (strengthening); the red area represents $d\theta'/dt' < 0$ (weakening); and the blue area represents $d\theta'/dt' \simeq 0$ (nearly steady state).

When $v' \gg 2c_s'a/G'$, the change in the slip velocity (dv'/dt') is governed by radiation damping. This never occurs in the SE regime but does in the OE regime after nucleation. We confirmed that separation of the two regimes depends on the value of l_{RA}. A value of l_{RA} lower than approximately 0.7 leads to the OE regime and $l_{RA} > 1.0$ leads to the SE regime. The dependence of these regimes on l_{RA} corresponds to the results obtained with the two-dimensional model in *Rubin* [2008]. Next, we found that the dependence of S_{n1}, R_{n1}, S_{n2}, and R_{n2} on the non-dimensional frictional parameters l_b and l_{b-a} in the OE regime are different from those in the SE regime.

Figures 5 and 6 show the dependence of S_{n1}, R_{n1}, S_{n2}, and R_{n2} on l_b, l_{b-a}, and l_{RA} in the OE regime. The numerical results imply that S_{n1} and S_{n2} (R_{n1} and R_{n2}) depend on l_{b-a} and l_b, but there seems to be no clear dependence on l_{RA}. We fit the results to the data using $R_n \propto (l_b)$ and $R_n \propto (l_{b-a})$. The reason for assuming this type of fitting will be discussed in Section 4.

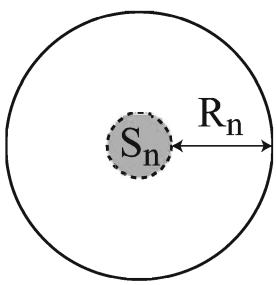

Figure 4. Schematic of the relation between the locking center area S_n and the characteristic length from the fault edge to the creep front, R_n, for a circular fault. R_n is defined as $1 - \sqrt{S_n}$. We measure S_{n1} (and R_{n1}) when the maximum slip velocity is 10 times the loading rate, and S_{n2} (and R_{n2}) when the maximum slip velocity is 100 times the loading rate.

As mentioned above, numerical experiments showed that the parameter dependence in the SE regime differ from those in the OE regime. All of the results are described in Table 2. Figure 7 shows the dependence of S_{n1} (and R_{n1}) on l_b, l_{b-a}, and l_{RA}. S_{n1} (and R_{n1}) can no longer be fitted with the lines used in the OE regime (see Figure 5). The results imply that the early phase of nucleation in the SE regime tends to be distributed over wider ranges than in the OE regime.

3.1.2. In the case of the slip law

In this section, we present the results obtained with the slip law ($d\theta'/dt' = -\ln(v'\theta'/L')v'\theta'/L'$).

First, we confirm that almost none of the ranges for the SE regime are present. For all practical purposes, only the OE regime exists. This tendency of the slip law was also reported in *Rubin* [2008]; this tendency might be pronounced in our model since the model does not contain any regions of velocity strengthening ($a/b > 1$). In order to cause spontaneous slow slip events to appear in a fault with the slip law, it is necessary to have rheological frictional heterogeneities (*Mitsui and Hirahara* [2008]) or evolution of pore fluid pressure (*Segall et al.* [2010]).

The results are presented in Table 3. Figures 8 and 9 show the dependence of S_{n1}, R_{n1}, S_{n2}, and R_{n2} on l_b, l_{b-a}, and l_{RA}. The numerical results imply that S_{n1} and S_{n2} (R_{n1} and R_{n2}) depend on l_b but are independent of l_{b-a} and l_{RA}. We fit the results to the data using R_{n1} and $R_{n2} \propto l_b$.

To support the above implication of the parameter dependence, we also present the results, using different symbols to specify the parameters, in Appendix A.

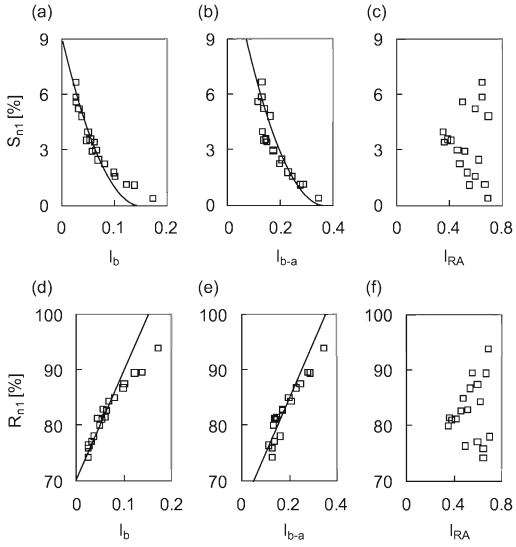

Figure 5. Dependence of S_{n1} and R_{n1} on the parameters for a circular fault in the case of the aging law in the OE regime. The open squares represent the results of numerical calculations. (a) and (d) Results for l_b. The solid line is a fitting line: $R_{n1} = 0.7 + 2l_b$. (b) and (e) Results for l_{b-a}. The solid line is a fitting line: $R_{n1} = 0.63 + l_{b-a}$. (c) and (f) Results for l_{RA}.

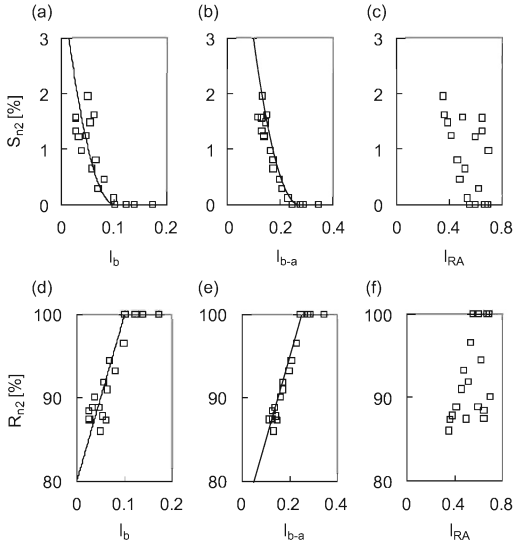

Figure 6. Dependence of S_{n2} and R_{n2} on the parameters for a circular fault in the case of the aging law in the OE regime. The open squares represent the results of numerical calculations. (a) and (d) Results for l_b. The solid line is a fitting line: $R_{n1} = 0.8 + 2l_b$. (b) and (e) Results for l_{b-a}. The solid line is a fitting line: $R_{n2} = 0.73 + l_{b-a}$. (c) and (f) Results for l_{RA}.

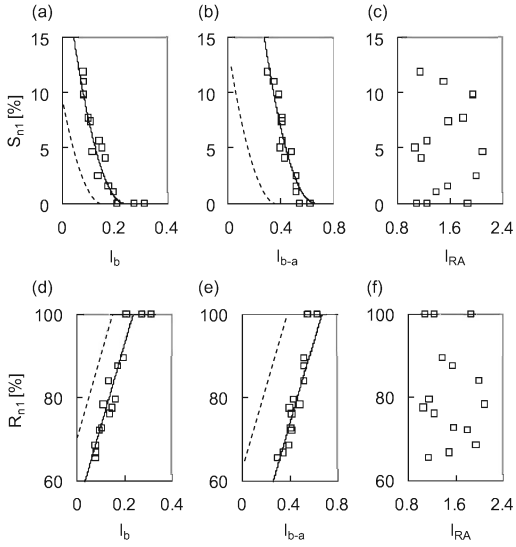

Figure 7. Dependence of S_{n1} and R_{n1} on the parameters for a circular fault in the case of the aging law in the SE regime. The open squares represent the results of numerical calculations. The dotted lines represent the fitting lines for the OE regime shown in Figure 5. (a) and (d) Results for l_b. The solid line is a fitting line: $R_{n1} = 0.53 + 2l_b$. (b) and (e) Results for l_{b-a}. The solid line is a fitting line: $R_{n1} = 0.34 + l_{b-a}$. (c) and (f) Results for l_{RA}.

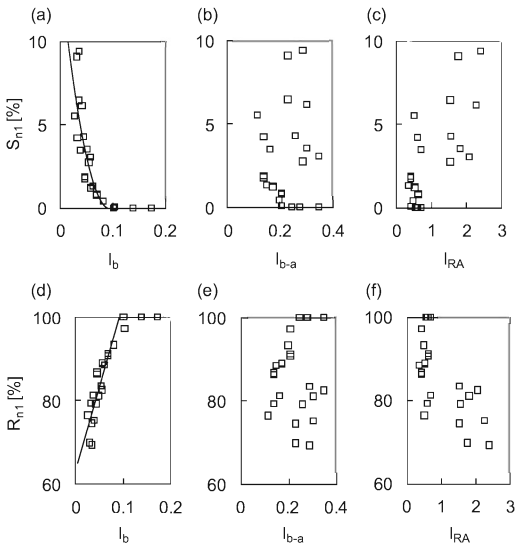

Figure 8. Dependence of S_{n1} and R_{n1} on the parameters for a circular fault in the case of the slip law. The open squares represent the results of numerical calculations. (a) and (d) Results for l_b. The solid line is a fitting line: $R_{n1} = 0.63 + 4l_b$. (b) and (e) Results for l_{b-a}. (c) and (f) Results for l_{RA}.

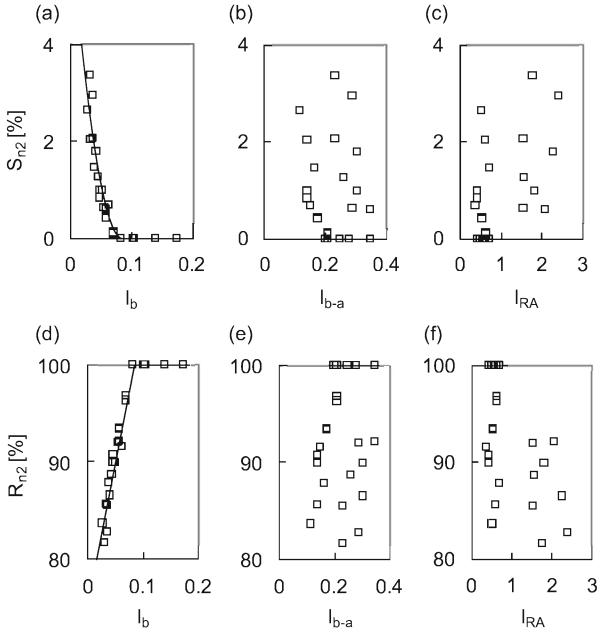

Figure 9. Dependence of S_{n2} and R_{n2} on the parameters for a circular fault in the case of the slip law. The open squares represent the results of numerical calculations. (a) and (d) Results for l_b. The solid line is a fitting line: $R_{n1} = 0.75 + 3l_b$. (b) and (e) Results for l_{b-a}. (c) and (f) Results for l_{RA}.

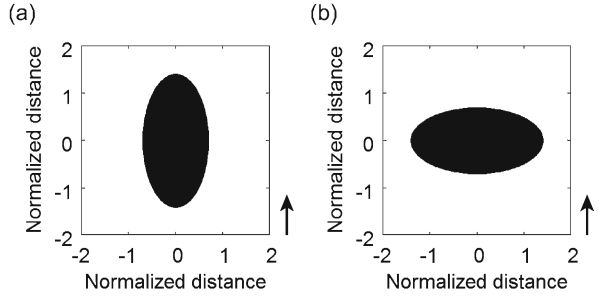

Figure 10. Cross sections of the elliptical faults along the fault surface shown in Figure 1(b). The black areas represent the fault patches, and the arrows indicate the loading directions. (a) Case of LM2. (b) Case of LM3.

3.2. Elliptical faults

Next, we consider elliptical faults, for which the ratio of the long radius to the short radius is 2. The area is assumed to be equal to that of a circular fault. The long radius is therefore $\sqrt{2}R$ and the short radius is $R/\sqrt{2}$, where R is equivalent to the oval radius. Moreover, we construct two models. In one of the models, the direction of the long radius is parallel to the loading direction, and we refer to this model as LM2 (long radius along mode-2 direction). In the other model, the direction of the long radius is perpendicular to the loading direction, and it is named LM3 (long radius along mode-3 direction). The two fault models are illustrated in Figure 10. S_n (S_{n1} and S_{n2}) and R_n (R_{n1} and R_{n2}) for an elliptical fault are measured as in the case of a circular fault (Figure 11).

We also perform some calculations for elliptical faults with the aging law in both the OE and SE regimes, and with the slip law. The data sets for the frictional parameters are chosen from the cases of a circular fault. The results are listed in Tables 4 and 5.

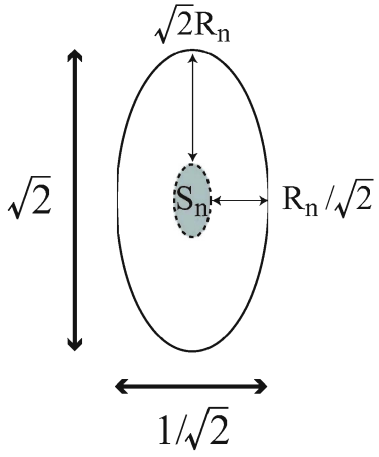

Figure 11. Schematic of the relation between the locking center area S_n and the characteristic length from the fault edge to the creep front, R_n, for an elliptical fault. As above, R_n is defined as $1 - \sqrt{S_n}$.

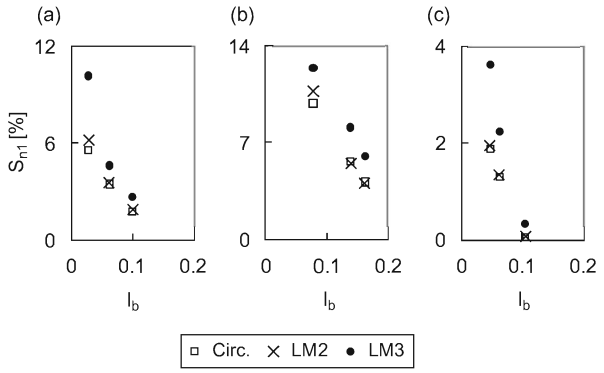

Figure 12. Dependence of S_{n1} on l_b. The open squares represent the results for a circular fault; the crosses, for an LM2 fault; and the solid circles, for an LM3 fault. (a) Case of the aging law in the OE regime. (b) Case of the aging law in the SE regime. (c) Case of the slip law.

Figure 12 shows the dependence of S_{n1} on l_b with the aging law in the OE and SE regimes, and with the slip law, which were used to check the effects of the fault shape. We found that the results for the LM3 fault are clearly different from those for the LM2 fault and for the circular fault. Namely, S_{n1} for the LM3 fault is larger than that for the circular fault, but the values for the LM2 fault and the circular fault are almost the same.

3.3. "Creep" propagation imposed by state variable evolution

We measured S_n (and R_n) as characteristic sizes in the early phase of nucleation. The sizes reflect the characteristics of creep propagation from the fault edge; Figure 13 shows an example of propagation of the creep front from the fault edge. The propagation velocity v'_{prop} gradually increases with propagation, which is associated with the increase in slip velocity at the creep front. As explained in Appendix B, the propagation velocity v'_{prop} is first approximated by Eq. (B1).

Only in the case of a fault governed by the aging law do the characteristic sizes also depend on l_{b-a} (Figures 5–7).

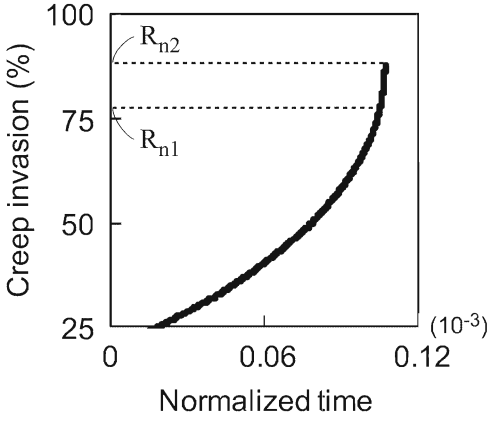

Figure 13. Example of creep front propagation for $l_b = 0.037$, $l_{b-a} = 0.16$, and $l_{RA} = 0.694$ (the same case as in Figure 2). The vertical axis represents the distance of the creep front from the fault edge divided by R. The line is plotted until the point where the slip rate at the front reaches $100v_0$. The upper value corresponds to R_{n2}.

In order to explain the dependence of l'_{b-a} in the case of the aging law, we propose a possible condition governing the creep front (instability front), namely, $d^2\theta'/dt'^2 = 0$. Since $d\theta'/dt'$ must be positive in front of the instability front, negative around it, and positive behind it (see Figure 3 as an example), $d^2\theta'/dt'^2$ should be zero around the front. We then write θ' and v' at that point as θ'_{af} and v'_{af}. From the state evolution of the aging law (Eq. (5)), $d^2\theta'_{af}/dt'^2 = 0$ can be rewritten as

$$\frac{d^2\theta'_{af}}{dt'^2} = \frac{-v'_{af} + v'^2_{af}\theta'_{af}/L' - \theta'_{af}(dv'_{af}/dt')}{L'} = 0 \quad (12)$$

Here, by taking the respective time derivatives of Eqs. (7) and (8), and excluding the radiation-damping term, we obtain

$$\frac{dv'_{af}}{dt'} = v'_{af}\left[\frac{d\tau'_{af}/dt'}{a} - \frac{b(d\theta'_{af}/dt')}{a\theta'_{af}}\right] \quad (13)$$

Next, substituting Eq. (13) into (12), the slip velocity at the point is obtained:

$$v'_{af} = \frac{L'[(b-a)/\theta'_{af} - d\tau'_{af}/dt']}{b-a} \quad (14)$$

This relation might lead to the dependence on $b-a$ of the fault governed by the aging law. For example, by assuming $v'_{front} \simeq v'_{af}$ in Eq. (B1), we arrive at

$$v'_{prop} \simeq \frac{L'[(b-a)/\theta'_{af} - d\tau'_{af}/dt']G'}{b(b-a)\ln(\theta'_{ini}[(b-a)/\theta'_{af} - d\tau'_{af}/dt']/(b-a))} \quad (15)$$

Although Eq. (15) still indicates complex parameter dependence, we can reduce it using the relations $l_b = G'L'/b$ and $l_{b-a} = G'L'/(b-a)$ as follows:

$$v'_{prop} \simeq l_b\left[\frac{[(b-a)/\theta'_{af} - d\tau'_{af}/dt']}{(b-a)\ln(\theta'_{ini}[(b-a)/\theta'_{af} - d\tau'_{af}/dt']/(b-a))}\right] \quad (16)$$

$$v'_{prop} \simeq l_{b-a}\left[\frac{[(b-a)/\theta'_{af} - d\tau'_{af}/dt']}{b\ln(\theta'_{ini}[(b-a)/\theta'_{af} - d\tau'_{af}/dt']/(b-a))}\right] \quad (17)$$

This implies the following approximate relations: $v'_{prop} \propto l_b$ or $v'_{prop} \propto l_{b-a}$. In fact, our results regarding R_{n2} (S_{n2}) in the OE regime in Figure 6 imply $R_n \propto l_{b-a}$, and R_{n1} (S_{n1}) in the SE regime in Figure 7 implies both $R_n \propto l_b$ and $R_n \propto l_{b-a}$.

For a fault governed by the slip law, we can adopt the same strategy. In the case of the slip law (Eq. (6)), $d\theta'_{af}/dt'^2 = 0$ is changed to

$$\frac{d^2\theta'_{af}}{dt'^2} = \frac{[v'^2_{af}\theta'_{af}/L']\ln(v'_{af}\theta'_{af}/L') - \theta'_{af}(dv'_{af}/dt')}{L'} = 0 \quad (18)$$

Substituting Eq. (13) in (18), we obtain

$$\left[b - a\ln\left(\frac{v'_{af}\theta'_{af}}{L'}\right)\right]v'_{af} = L'\left(\frac{b}{\theta'_{af}} - \frac{d\tau'_{af}}{dt'}\right) \quad (19)$$

Next, by comparing Eq. (19) with Eq. (14), it becomes clear why there are no $b-a$ dependence in the case of the slip law. Assuming $v'_{front} \simeq v'_{af}$ again, Eq. (B1) is modified as follows:

$$v'_{prop} \simeq \frac{L'[b/\theta'_{af} - d\tau'_{af}/dt']G'}{b[b - a\ln(v'_{af}\theta'_{af}/L')]\ln(\theta'_{ini}[b/\theta'_{af} - d\tau'_{af}/dt']/[b - a\ln(v'_{af}\theta'_{af}/L')])} \quad (20)$$

$$= l_b\left[\frac{[b/\theta'_{af} - d\tau_{af}'/dt']}{[b - a\ln(v'_{af}\theta'_{af}/L')]\ln(\theta'_{ini}[b/\theta'_{af} - d\tau'_{af}/dt']/[b - a\ln(v'_{af}\theta'_{af}/L')])}\right] \quad (21)$$

Indeed, an approximate relation $v'_{prop} \propto l_b$ might work for the slip law fault since $R_n \propto l_b$, as shown in Figures 8 and 9.

4. Discussion

4.1. Effects of l_{RA} in the case of the aging law

In our results using the aging law, l_{RA} determined the regime of the slip events; this corresponds with previous studies using two-dimensional models, as is explained in Appendix C. In our three-dimensional model, $l_{RA} < 0.7$ led to the OE regime, but $l_{RA} > 1.0$ led to the SE regime. We found that the characteristic sizes of early nucleation (R_n and S_n) depend on the regime (see Figure 7). R_n in the SE regime is smaller (in other words, S_n in the SE regime is larger) unless the maximum slip rate at the creep front does not reach the threshold value for measuring S_n. However, explaining this fact is rather difficult. We think that Eq. (B1) could provide a hint. Here, θ'_{ini} in Eq. (B1) represents the magnitude of the strength healing from the stress drop in a prior event. In addition, the slip velocity at the creep front in the SE regime always involves certain limits, which are considerably smaller than $2c'_s a/G'$. For example, many of our results for S_{n2} in the SE regime are 0 (Table 2), since $\log_{10}(v')$ never reaches 2 in these cases. This point will be clarified in future studies.

Moreover, the minimum value of l_{RA} we tested was 0.351. What happens in the case of $l_{RA} < 0.35$? We tried many calculations with this parameter range. However, all of the calculations showed that the mirror symmetry of slip evolution along the loading direction breaks, namely, slip instability, occurs disproportionately near the fault tip and high-speed slip propagates unidirectionally. Such breaking of the mirror symmetry was also shown in *Chen and Lapusta* [2009] (Figure 6 in their paper). This is not a physical result due to numerical instability, because the fault is assumed to have mirror symmetry along the loading direction. We also tried calculations with smaller grid sizes and the same frictional parameters, but the results did not change. Therefore, we concluded that $l_{RA} < 0.35$ leads to breaking of the mirror symmetry, resulting in earlier nucleation than in other cases. This limitation would be important in discussing numerical results for faults with more complex distributions of frictional parameters.

We further confirmed that the regime classified by l_{RA} is almost consistent with the calculation results in a previous study with an inertial effect and a velocity-strengthening region surrounding the velocity-weakening patch (*Chen and Lapusta* [2009]). The results shown in Figure 3 in *Chen and Lapusta* [2009], $l_{RA} \approx 0.92$, seem to correspond to the SE regime; those shown in Figure 5, $l_{RA} = 0.76$, correspond to the OE regime; and those shown in Figure 6, $l_{RA} \approx 0.33$, correspond to the case where breaking of the mirror symmetry occurs. (Note that we did not show the cases for the regime transition range ($0.7 < l_{RA} < 1.0$) in this study, since these led to complex fault behavior.)

4.2. Effects of fault geometry

We found that the direction of the fault loading affects nucleation. Figure 12 shows that S_{n1} for an LM3 fault is larger than those for circular and LM2 faults, for both the state evolution laws. The difference between the loading directions of the LM2 and LM3 faults notably affects the early phase of nucleation.

In order to illustrate a particular example, Figure 14 shows snapshots of the early phase of nucleation for LM2 and LM3 faults with the same frictional parameters. In the case of the LM2 fault, the nucleation shape looks similar to the fault shape as well as the shape in the case of a circular fault. By contrast, in the case of the LM3 fault, the nucleation shape looks different from that of the fault shape. This may lead to the above characteristics in the case of the LM3 fault. Moreover, especially in the case of the aging law, we confirm by some trial calculations that the parameter range for the SE regime in the case of the LM3 fault is apparently larger (Z, which is defined in Appendix C, is smaller) than in the case of the circular fault.

One possible explanation for this point is that evolution of slip instability is determined by the minimum dimension of the ellipse. The section along the minor axis of the LM2 fault corresponds to a mode-3 direction, whereas that of the LM3 fault corresponds to a mode-2 direction. Since, in general, the effective rigidity for elastic deformation in a mode-2 direction is larger than the rigidity (a multiple of $1/(1-P_o)$, where P_o is Poisson's ratio), nucleation just before dynamic instability should require a larger dimension in the mode-2 direction (this is identical to the nucleation area shown in Figure 2(d)). This would affect the early phase of nucleation. On the LM3 fault, because the minor axis corresponds to the mode-2 direction, the larger dimension of nucleation along the minor axis may lead to earlier instability occurrence, a shorter R_n, and a larger S_n.

Such characteristics might cause differences between large strike-slip faults (LM2-like) and dip-slip faults (LM3-like) as subducting plate boundaries.

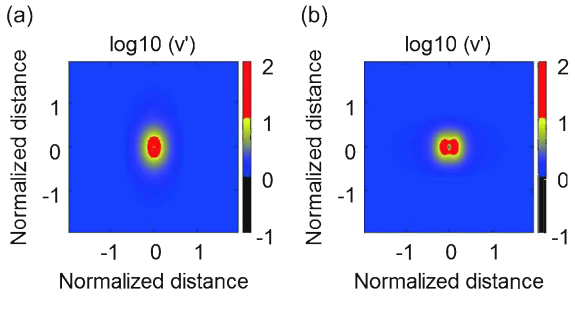

Figure 14. Snapshots of early nucleation when $\log_{10} v'$ reaches 2, in the case of the slip law for $l_b = 0.206$, $l_{b-a} = 0.103$, and $l_{RA} = 0.412$. (a) Case of LM2. (b) Case of LM3.

4.3. Implications for actual faults

During the early phase of nucleation in our model, the creep front propagates from the fault edges into the locking center area, depending on the value of l_b (and also l_{b-a} in the case of the aging law). This means that nucleation definitely depends on fault sizes, since l_b is inversely proportional to the characteristic fault length R. In addition, if the characteristic length L for the state evolution is assumed to be proportional to R, the early phase of nucleation behaves as a scale-independent (self-similar) phenomenon, although such an assumption is sophistic.

Moreover, we obtained fitting of the results to the calculation data using $R_n \propto l_b$ and $R_n \propto l_{b-a}$, as shown in Figures 5–9. However, these depend on our assumptions of simple fault geometries, homogeneities of the parameters within the velocity-weakening region, and steady slip outside the region. The fitting lines would be inappropriate for application to actual faults.

Instead, the important implications of our results for actual faults are as follows. The early phase of nucleation is certainly controlled by $R_n \propto l_b$ and $R_n \propto l_{b-a}$, where the values of l_b and l_{b-a} are local values around the inward creep front. After this early phase, however, inward propagation is masked by the increase in the slip rate within the locking center area due to stress concentration. This later phase is no longer controlled by the above relations (for example, the OE and SE regimes in the case of the aging law, separated by the value of l_{RA}). In particular, heterogeneities of the frictional parameters may allow local stress to concentrate highly and lead to an earlier occurrence of unstable slip events than in a homogeneous model. In other words, R_{n1} and R_{n2} can be shortened by fault heterogeneities. Furthermore, introduction of a velocity-strengthening region surrounding the velocity-weakening patch might affect early nucleation. *Kato* [2008] showed several examples of model calculations on such faults with heterogeneities. We are on the way to understanding the whole system for applying the model to actual faults.

5. Conclusion

We investigated the dependence of the size of early nucleation on various parameters for homogeneous faults. We assumed the rate- and state-dependent law as a constitutive friction law, with both the aging and slip laws. The parameter range in which we performed the experiments was $a/b \geq 0.5$. To focus on the early phase of nucleation, we defined S_n as the relative size of a locking center area with respect to the entire fault, and $R_n = 1 - \sqrt{S_n}$ as the invasion distance of an inward creep. When the slip velocity at the creep front became 10 times the loading rate, we measured S_{n1} (R_{n1}); when it became 100 times the loading rate, we measured S_{n2} (R_{n2}).

First, for a circular fault, we were able to compile the dependence of S_n and R_n on the dimensionless parameters l_b, l_{b-a}, and l_{RA}. For faults governed by the aging law, we classify the results into two regimes, depending on the value of l_{RA}. One regime is referred to as the OE (ordinary events) regime, which is characterized by $l_{RA} < 0.7$, and the other, named the SE (slow events) regime, corresponds to $l_{RA} > 1$. In both regimes, R_n is proportional to l_b and l_{b-a}. Moreover, the regimes have different trend lines (Figure 7), although we could not investigate this for the case of $l_{RA} < 0.35$ because of breaking of the mirror symmetry of the slip instability along the loading direction. R_n in the SE regime is smaller (in other words, S_n in the SE regime is larger) than in the OE regime unless the maximum slip rate at the creep front does not reach the threshold value for measuring S_n. Furthermore, in faults obeying the slip law, there is practically no SE regime. In this case, R_n is proportional to l_b but independent of l_{b-a}. The reason for the apparent dependence of R_n on l_b (both aging and slip laws) as well as on l_{b-a} (aging law) can be partly explained in terms of the propagation velocity of the inward creep front.

Next, we investigated the differences between elliptical and circular faults. We constructed the LM2 model (long radius along mode-2 direction) and the LM3 model (long radius along mode-3 direction), and found that they are clearly different. For LM2 faults, the parameter dependence of early nucleation is similar to that for circular faults, but that for LM3 faults is different. Furthermore, in the case of LM3 faults, R_n is smaller (thus S_n for LM3 faults is larger), and it was found that the direction of the fault loading does indeed affect early nucleation.

Our results imply that the fault instability parameters (particularly l_b) can be qualitatively estimated from the early phase of nucleation. However, the parameter dependence are not simple, even for modeled faults, since they display fundamental relations with the state evolution law and the fault geometry. Furthermore, they can be drastically affected by fault heterogeneities. More studies are necessary before this approach can be applied to actual faults.

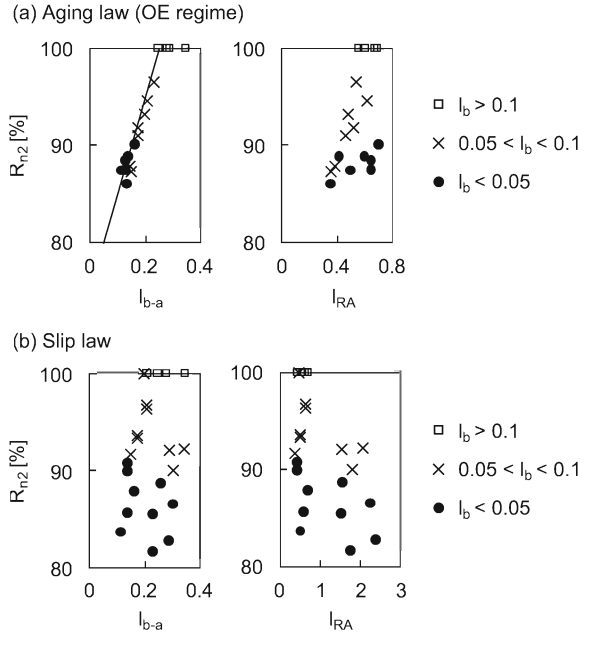

Figure 15. Dependence of R_{n2} on l_{b-a} and l_{RA} for a circular fault, using different symbols, in response to the value of l_b. (a) Case of the aging law in the OE regime (corresponding to Figures 6(e) and (f)). (b) Case of the slip law (corresponding to Figures 9(e) and (f)).

Appendix A: Results with specifying parameters

Figures 5–9 show the compiled results for the parameters listed in Table 1–3. However, they do not concisely display the parameter range. To achieve this, we show the results, using different symbols, in response to the value of l_b because l_b was related to early nucleation in all cases.

Figure 15 shows the dependence of l_{b-a} and l_{RA} on R_{n2} again, for both the aging law (OE regime) and the slip law. We can reconfirm that only l_{b-a} in the case of the aging law has a clear dependence on R_{n2}.

Appendix B: General expression of "creep" propagation

As some studies have shown (e.g., *Ida* [1973]; *Ampuero and Rubin* [2008]), the propagation velocity v'_{prop} is generally expressed as $v'_{prop} = dz'/dt' = (du'/dt')(dz'/du') = v'_{front}(dz'/du')$, where z' is the spatial coordinate of the creep front and v'_{front} is the slip velocity at the front. Furthermore, dz'/du' is of the order of $G'/\Delta\tau'_f$ since $\Delta\tau'_f \simeq G'(du'/dz')$, where $\Delta\tau'_f$ is the stress drop from its peak value around the front. The difference of Eqs. (1) and (3) yields $\Delta\tau'_f \simeq b\ln(v'_{front}\theta'_{ini}/L')$, where θ'_{ini} is the state variable immediately in front of the creep front. The propagation velocity v'_{prop} is therefore approximated as follows:

$$v'_{prop} \simeq \frac{v'_{front}G'}{b\ln(v'_{front}\theta'_{ini}/L')} \tag{B1}$$

Thus, the creep propagation velocity v'_{prop} fundamentally depends on b, v'_{front}, θ'_{ini}, and L'.

Qualitatively, a larger b (smaller l_b) leads to a slower v'_{prop}, smaller R_n, and larger S_n, corresponding to our results (Figures 5–9).

Appendix C: Differences between the OE and SE regimes

As described above, nucleation in the case of a fault governed by the aging law is divided into two regimes, depending on the value of l_{RA}. This division can be explained by introducing the Griffith criterion $G'_c = G'_r$ from fracture mechanics, as described in *Rubin and Ampuero* [2005]; *Ampuero and Rubin* [2008]; *Rubin* [2008], where G'_c is the (normalized) effective fracture energy and G'_r is the (normalized) energy release rate. The point here is that G'_c depends on the stress drop from its peak value $\Delta\tau'_f \simeq b\ln(v'_{front}\theta'_{ini}/L')$, but G'_r depends on the stress drop from its ambient value $\Delta_a\tau'_f \simeq (b-a)\ln(v'_{front}\theta'_{ini}/L')$. In the case of the aging law, which behaves as linear slip weakening (*Cocco and Bizzarri* [2002], the weakening rate is $\sim b/L'$) and G'_c is approximated as follows:

$$G'_c = \frac{\Delta\tau'^2_f L'}{2b} \tag{C1}$$

G'_r is the multiple of the slip increment and $\Delta_a\tau'_f$ at the creep front. Let us consider a quasi-circular slip front expanding outwards from the fault center (with normalized radius R'_s). The slip around the fault center can be represented as $ZR'_s\Delta_a\tau'_f/G'$ (remember that the effective stiffness is $\propto G'$). Further, Z has a constant value. Then, G'_r is given as $ZR'_s\Delta_a\tau'^2_f/G'$. The Griffith criterion $G'_c = G'_r$ determines the following threshold value R'_c:

$$ZR'_c = \frac{G'L'\Delta\tau'^2_f}{b\Delta_a\tau'^2_f} = \frac{G'L'b^2}{b(b-a)^2} = l_{RA} \tag{C2}$$

When $R'_s > R'_c$, the slip front can expand unstably. In such cases, the slip velocity at the front would easily exceed $2c'_s a/G'$ and can be restrained by radiation damping. This is the OE regime. In contrast, when $R'_s < R'_c$, the slip velocity at the front evolves more moderately. Specifically, $1 < R'_c$ ($Z < l_{RA}$) leads to a moderate slip event over the fault (care should be taken with regard to $R'_s < R' = 1$). Therefore, $Z < l_{RA}$ becomes the definition of the SE regime, and $Z > l_{RA}$ is the definition of the OE regime. Our results indicate Z : 0.7-1.0 for a circular fault, and this value can be changed for elliptical faults. This will be investigated in future studies.

Acknowledgments. This manuscript was improved by helpful discussions and comments by Yoshihisa Iio, Hikaru Kawamura, Masajiro Imoto, Jean-Paul Ampuero, Takeshi Sagiya, and Chihiro Hashimoto. We benefit from detailed and effective comments by anonymous reviewers. This research has been supported primarily by the Japan Society for the Promotion of Science (20-230) and a Grant-in-Aid for Scientific Research (B) (20340119) from MEXT.

References

Ampuero, J.-P., and A. M. Rubin (2008), Earthquake nucleation on rate and state faults -Aging and slip laws, *J. Geophys. Res.*, *113*(B1), doi:10.1029/2007JB005082.

Ben-Zion, Y., and J. R. Rice (1995), Slip patterns and earthquake populations along different classes of faults in elastic solids, *J. Geophys. Res.*, *100*(B7), 12,959, doi:10.1029/94JB03037.

Bizzarri, A., M. Cocco, D. J. Andrews, and E. Boschi (2001), Solving the dynamic rupture problem with different numerical approaches and constitutive laws, *Geophys. J. Int.*, *144*(3), 656–678, doi:10.1046/j.1365-246x.2001.01363.x.

Boatwright, J., and M. Cocco (1996), Frictional constraints on crustal faulting, *J. Geophys. Res.*, *101*(B6), 13,895–13,909, doi:10.1029/96JB00405.

Brune, J. N. (1970), Tectonic Stress and the Spectra of Seismic Shear Waves from Earthquakes, *J. Geophys. Res.*, *75*(26), 4997–5009, doi:10.1029/JB075i026p04997.

Chen, T., and N. Lapusta (2009), Scaling of small repeating earthquakes explained by interaction of seismic and aseismic slip in a rate and state fault model, *J. Geophys. Res.*, *114*(B1), doi:10.1029/2008JB005749.

Cocco, M., and A. Bizzarri (2002), On the slip-weakening behavior of rate- and state dependent constitutive laws, *Geophys. Res. Lett.*, *29*(11), doi:10.1029/2001GL013999.

Day, S. M. (1982), Three-dimensional simulation of spontaneous rupture: The effect of nonuniform prestress, *Bull. Seis. Soc. Am.*, *72*(6), 1881–1902.

Dieterich, J. H. (1979), Modeling of Rock Friction 1. Experimental Results and Constitutive Equations, *J. Geophys. Res.*, *84*(B5), 2161–2168, doi:10.1029/JB084iB05p02161.

Dieterich, J. H. (1986), A model for the nucleation of earthquake slip, in *Earthquake source mechanics, AGU Geophysical Monograph 37*, vol. 6, edited by S. Das, J. Boatwright, and C. H. Scholz, pp. 37–47.

Dieterich, J. H. (1992), Earthquake nucleation on faults with rate- and state-dependent strength, *Tectonophysics*, *211*(1-4), 115–134, doi:10.1016/0040-1951(92)90055-B.

Fukuyama, E., and R. Madariaga (1998), Rupture dynamics of a planar fault in a 3D elastic medium: Rate- and slip- weakening friction, *Bull. Seis. Soc. Am.*, *88*(1), 1–17.

Helmstetter, A., and B. E. Shaw (2009), Afterslip and aftershocks in the rate-and-state friction law, *J. Geophys. Res.*, *114*(B1), doi:10.1029/2007JB005077.

Hori, T., N. Kato, K. Hirahara, T. Baba, and Y. Kaneda (2004), A numerical simulation of earthquake cycles along the Nankai Trough in southwest Japan: lateral variation in frictional property due to the slab geometry controls the nucleation position, *Earth Planet. Sci. Lett.*, *228*(3-4), 215–226, doi:10.1016/j.epsl.2004.09.033.

Ida, Y. (1972), Cohesive Force across the Tip of a Longitudinal-Shear Crack and Griffith's Specific Surface Energy, *J. Geophys. Res.*, *77*(20), 3796–3805, doi:10.1029/JB077i020p03796.

Ida, Y. (1973), The maximum acceleration of seismic ground motion, *Bull. Seis. Soc. Am.*, *63*(3), 959–968.

Kaneko, Y., and N. Lapusta (2008), Variability of earthquake nucleation in continuum models of rate-and-state faults and implications for aftershock rates, *J. Geophys. Res.*, *113*(B12), doi:10.1029/2007JB005154.

Kato, N. (2003), Repeating slip events at a circular asperity: Numerical simulation with a rate- and state- dependent friction law, *Bull. Earthq. Res. Inst.*, *78*, 151–166.

Kato, N. (2008), How Frictional Properties Lead to Either Rupture-Front Focusing or Cracklike Behavior, *Bull. Seis. Soc. Am.*, *97*(6), 2182–2189, doi:10.1785/0120070037.

Kato, N., and T. E. Tullis (2001), A composite rate- and state-dependent law for rock friction, *Geophys. Res. Lett.*, *28*(6), 1103, doi:10.1029/2000GL012060.

Lapusta, N., and Y. Liu (2009), Three-dimensional boundary integral modeling of spontaneous earthquake sequences and aseismic slip, *J. Geophys. Res.*, *114*(B9), doi:10.1029/2008JB005934.

Lapusta, N., and J. R. Rice (2003), Nucleation and early seismic propagation of small and large events in a crustal earthquake model, *J. Geophys. Res.*, *108*(B4), doi:10.1029/2001JB000793.

Liu, Y., and J. R. Rice (2005), Aseismic slip transients emerge spontaneously in three-dimensional rate and state modeling of subduction earthquake sequences, *J. Geophys. Res.*, *110*(B8), doi:10.1029/2004JB003424.

Madariaga, R. (1976), Dynamics of an expanding circular fault, *Bull. Seis. Soc. Am.*, *66*(3), 639–666.

Marone, C. J., C. H. Scholtz, and R. Bilham (1991), On the Mechanics of Earthquake Afterslip, *J. Geophys. Res.*, *96*(B5), 8441–8452, doi:10.1029/91JB00275.

Mikumo, T., and T. Miyatake (1978), Dynamical rupture process on a three-dimensional fault with non-uniform frictions and near-field seismic waves, *Geophys. J. R. Astr. Soc.*, *54*(2), 417–438, doi:10.1111/j.1365-246X.1978.tb04267.x.

Mitsui, Y., and K. Hirahara (2008), Long-term slow slip events are not necessarily caused by high pore fluid pressure at the plate interface: an implication from two-dimensional model calculations, *Geophys. J. Int.*, *174*(1), 331–335, doi:10.1111/j.1365-246X.2008.03832.x.

Miyazaki, S., P. Segall, J. J. McGuire, T. Kato, and Y. Hatanaka (2006), Spatial and temporal evolution of stress and slip rate during the 2000 Tokai slow earthquake, *J. Geophys. Res.*, *111*(B3), doi:10.1029/2004JB003426.

Nakatani, M., and C. H. Scholz (2004), Frictional healing of quartz gouge under hydrothermal conditions: 2. Quantitative interpretation with a physical model, *J. Geophys. Res.*, *109*(B7), doi:10.1029/2003JB002938.

Perfettini, H., and J.-P. Ampuero (2008), Dynamics of a velocity strengthening fault region: Implications for slow earthquakes and postseismic slip, *J. Geophys. Res.*, *113*(B9), doi:10.1029/2007JB005398.

Press, W. H., B. P. Teukolsky, and W. T. Vetterling (1992), *Numerical Recipes*, 2nd ed., Cambridge University Press, New York.

Rice, J. R. (1993), Spatio-temporal Complexity of Slip on a Fault, *J. Geophys. Res.*, *98*(B6), 9885–9907, doi:10.1029/93JB00191.

Rubin, A. M. (2008), Episodic slow slip events and rate-and-state friction, *J. Geophys. Res.*, *113*(B11), doi:10.1029/2008JB005642.

Rubin, A. M., and J.-P. Ampuero (2005), Earthquake nucleation on (aging) rate and state faults, *J. Geophys. Res.*, *110*(B11), doi:10.1029/2005JB003686.

Ruina, A. (1980), Friction laws and instabilities: A quasistatic analysis of some dry frictional behavior, Ph.D. thesis, Cornell University.

Ruina, A. (1983), Slip Instability and State Variable Friction Laws, *J. Geophys. Res.*, *88*(B12), 10,359–10,370, doi:10.1029/JB088iB12p10359.

Savage, J. C. (1983), A Dislocation Model of Strain Accumulation and Release at a Subduction Zone, *J. Geophys. Res.*, *88*(B6), 4984–4996, doi:10.1029/JB088iB06p04984.

Savage, J. C., and J. Langbein (2008), Postearthquake relaxation after the 2004 M6 Parkfield, California, earthquake and rate-and-state friction, *J. Geophys. Res.*, *113*(B10), doi:10.1029/2008JB005723.

Segall, P., A. M. Rubin, A. M. Bradley, and J. R. Rice (2010), Dilatant strengthening as a mechanism for slow slip events, *J. Geophys. Res.*, *115*(B12), doi:10.1029/2010JB007449.

Tinti, E., A. Bizzarri, and M. Cocco (2005), Modeling the dynamic rupture propagation on heterogeneous faults with rate- and state-dependent friction, *Annals. Geophys.*, *48*(2), 327–345.

Tse, S. T., and J. R. Rice (1986), Crustal Earthquake Instability in Relation to the Depth Variation of Frictional Slip Properties, *J. Geophys. Res.*, *91*(B9), 9452–9472, doi: 10.1029/JB091iB09p09452.

Yuta Mitsui
Department of Geophysics, Graduate School of Science, Kyoto University, Kitashirakawa-Oiwakecho, Sakyo-ku, Kyoto 606-8502, Japan (mitsui@kugi.kyoto-u.ac.jp)

Table 1. Results for a circular fault with the aging law in the OE regime. The parameter ranges of the trials are as follows: $0.004 < a < 0.04$, $0.005 < b < 0.05$, $0.001 < b - a < 0.01$, $0.375 \times 10^{-6} < L' < 6 \times 10^{-6}$, $0.114 < l_{b-a} < 0.343$, $0.026 < l_b < 0.172$, and $0.351 < l_{RA} < 0.694$.

case	a	b	L' ($\times 10^{-6}$)	l_{b-a}	l_b	l_{RA}	S_{n1} [%]	S_{n2} [%]	R_{n1} [%]	R_{n2} [%]
1	0.01	0.013	1.4	0.160	0.037	0.694	4.83	0.98	78.0	90.1
2	0.01	0.013	1.2	0.137	0.032	0.595	5.22	1.23	77.1	88.9
3	0.01	0.013	1	0.114	0.026	0.495	5.59	1.58	76.4	87.4
4	0.01	0.017	5	0.245	0.101	0.595	1.58	0	87.4	100
5	0.01	0.017	4	0.196	0.081	0.476	2.26	0.46	85.0	93.3
6	0.01	0.017	3	0.147	0.061	0.357	3.44	1.61	81.5	87.3
7	0.02	0.03	6	0.206	0.069	0.617	2.47	0.30	84.3	94.6
8	0.02	0.03	5	0.172	0.057	0.515	2.91	0.66	82.9	91.9
9	0.02	0.03	4	0.137	0.046	0.412	3.53	1.24	81.2	88.8
10	0.005	0.008	1.5	0.172	0.064	0.457	2.98	0.81	82.7	91.0
11	0.005	0.008	1.25	0.143	0.054	0.381	3.59	1.49	81.1	87.8
12	0.005	0.008	1.15	0.131	0.049	0.351	3.99	1.96	80.0	86.0
13	0.005	0.01	5	0.343	0.172	0.686	0.39	0	93.8	100
14	0.005	0.01	4	0.274	0.137	0.549	1.10	0	89.5	100
15	0.004	0.005	0.375	0.129	0.026	0.643	6.64	1.57	74.2	87.5
16	0.04	0.05	3.75	0.129	0.026	0.643	5.84	1.33	75.8	88.5
17	0.008	0.014	5	0.286	0.123	0.667	1.12	0	89.4	100
18	0.008	0.014	4	0.229	0.098	0.533	1.77	0.12	86.7	96.6

Table 2. Results for a circular fault with the aging law in the SE regime. The parameter ranges of the trials are as follows: $0.004 < a < 0.04$, $0.005 < b < 0.05$, $0.001 < b - a < 0.01$, $1.125 \times 10^{-6} < L' < 12.6 \times 10^{-6}$, $0.294 < l_{b-a} < 0.617$, $0.076 < l_b < 0.309$, and $1.05 < l_{RA} < 2.08$.

case	a	b	L' ($\times 10^{-6}$)	l_{b-a}	l_b	l_{RA}	S_{n1} [%]	S_{n2} [%]	R_{n1} [%]	R_{n2} [%]
19	0.01	0.013	4.2	0.480	0.111	2.08	4.65	0	78.4	100
20	0.01	0.013	3.6	0.412	0.095	1.78	7.73	0	72.2	100
21	0.01	0.013	3	0.343	0.079	1.49	11.0	0.30	66.8	94.6
22	0.01	0.015	9	0.617	0.206	1.85	0	0	100	100
23	0.01	0.015	7.5	0.515	0.172	1.54	1.54	0	87.6	100
24	0.01	0.015	6	0.412	0.137	1.23	5.65	0	76.2	100
25	0.02	0.027	10.5	0.515	0.133	1.98	2.52	0	84.1	100
26	0.02	0.027	8.25	0.404	0.105	1.56	7.44	0	72.7	100
27	0.02	0.027	6	0.294	0.076	1.13	11.9	1.44	65.5	88.0
28	0.005	0.008	4.5	0.515	0.193	1.05	1.09	0	89.6	100
29	0.005	0.008	3.75	0.429	0.161	1.14	4.12	0	79.7	100
30	0.005	0.008	3.45	0.394	0.148	1.05	5.03	0	77.6	100
31	0.005	0.01	9	0.617	0.309	1.23	0	0	100	100
32	0.004	0.008	6.3	0.540	0.270	1.08	0	0	100	100
33	0.008	0.016	12.6	0.540	0.270	1.08	0	0	100	100
34	0.004	0.005	1.125	0.386	0.077	1.93	9.82	0	68.7	100
35	0.04	0.05	11.25	0.386	0.077	1.93	9.83	0	68.6	100

Table 3. Results for a circular fault with the slip law. The parameter ranges of the trials are as follows: $0.005 < a < 0.022$, $0.01 < b < 0.03$, $0.002 < b - a < 0.01$, $1 \times 10^{-6} < L' < 6 \times 10^{-6}$, $0.114 < l_{b-a} < 0.343$, $0.026 < l_b < 0.172$, and $0.357 < l_{RA} < 2.38$.

case	a	b	L' ($\times 10^{-6}$)	l_{b-a}	l_b	l_{RA}	S_{n1} [%]	S_{n2} [%]	R_{n1} [%]	R_{n2} [%]
36	0.01	0.013	1.4	0.160	0.037	0.694	3.47	1.47	81.4	87.9
37	0.01	0.013	1.2	0.137	0.032	0.595	4.24	2.04	79.4	85.7
38	0.01	0.013	1	0.114	0.026	0.495	5.53	2.66	76.5	83.7
39	0.01	0.015	3	0.206	0.069	0.617	0.85	0.13	90.8	96.4
40	0.01	0.015	2.5	0.172	0.057	0.515	1.23	0.44	88.9	93.4
41	0.01	0.015	2	0.137	0.046	0.412	1.88	1.00	86.3	90.0
42	0.01	0.017	5	0.245	0.101	0.595	0	0	100	100
43	0.01	0.017	4	0.196	0.081	0.476	0.44	0	93.3	100
44	0.01	0.017	3	0.147	0.061	0.357	1.31	0.70	88.6	91.7
45	0.02	0.03	6	0.206	0.069	0.617	0.76	0.10	91.3	96.9
46	0.02	0.03	5	0.172	0.057	0.515	1.21	0.41	89.0	93.6
47	0.02	0.03	4	0.137	0.046	0.412	1.78	0.85	86.7	90.8
48	0.005	0.01	5	0.343	0.172	0.686	0	0	100	100
49	0.005	0.01	4	0.274	0.137	0.549	0	0	100	100
50	0.005	0.01	3	0.206	0.103	0.412	0.07	0	97.4	100
51	0.022	0.025	2.5	0.286	0.034	2.38	9.41	2.96	69.3	82.8
52	0.013	0.015	1.75	0.300	0.040	2.25	6.13	1.80	75.2	86.6
53	0.013	0.016	2.5	0.286	0.054	1.52	2.74	0.63	83.4	92.0
54	0.017	0.02	2	0.229	0.034	1.52	6.46	2.08	74.6	85.6
55	0.02	0.023	2	0.229	0.030	1.75	9.09	3.36	69.9	81.7
56	0.01	0.012	2	0.343	0.057	2.06	3.05	0.61	82.5	92.2
57	0.01	0.012	1.75	0.300	0.050	1.80	3.53	1.00	81.2	90.0
58	0.01	0.012	1.5	0.257	0.043	1.54	4.30	1.27	79.3	88.7

Table 4. Results for an LM2 fault.

case	a	b	L' ($\times 10^{-6}$)	l_{b-a}	l_b	l_{RA}	S_{n1} [%]	S_{n2} [%]	R_{n1} [%]	R_{n2} [%]
Aging law in the OE regime										
3	0.01	0.013	1	0.114	0.026	0.495	6.15	1.63	75.2	87.2
6	0.01	0.017	3	0.147	0.061	0.357	3.50	1.59	81.3	87.4
18	0.008	0.014	4	0.229	0.098	0.533	1.89	0.13	86.3	96.4
Aging law in the SE regime										
23	0.01	0.015	6	0.412	0.137	1.23	5.47	0	76.6	100
28	0.005	0.008	3.75	0.429	0.161	1.14	4.03	0	79.9	100
34	0.04	0.05	11.25	0.386	0.077	1.93	10.7	0	67.3	100
Slip law										
41	0.01	0.015	2	0.137	0.046	0.412	1.96	0.98	86.0	90.1
44	0.01	0.017	3	0.147	0.061	0.357	1.35	0.67	88.4	91.8
50	0.005	0.01	3	0.206	0.103	0.412	0.07	0	97.3	100

Table 5. Results for an LM3 fault.

case	a	b	L' ($\times 10^{-6}$)	l_{b-a}	l_b	l_{RA}	S_{n1} [%]	S_{n2} [%]	R_{n1} [%]	R_{n2} [%
Aging law in the OE regime										
3	0.01	0.013	1	0.114	0.026	0.495	10.1	2.12	68.1	85.5
6	0.01	0.017	3	0.147	0.061	0.357	4.60	1.63	78.6	87.2
18	0.008	0.014	4	0.229	0.098	0.533	2.68	0.21	83.6	95.4
Aging law in the SE regime										
23	0.01	0.015	6	0.412	0.137	1.23	8.07	0	71.6	100
28	0.005	0.008	3.75	0.429	0.161	1.14	5.99	0	75.5	100
34	0.04	0.05	11.25	0.386	0.077	1.93	12.4	0	64.8	100
Slip law										
41	0.01	0.015	2	0.137	0.046	0.412	3.63	1.89	81.0	86.3
44	0.01	0.017	3	0.147	0.061	0.357	2.23	1.21	85.1	89.0
50	0.005	0.01	3	0.206	0.103	0.412	0.34	0	94.2	100